View metadata, citation and similar papers at core.ac.uk
brought to you by CORE
provided by Digital.CSIC

Real-Space Analysis of Branchpoint Motion in Architecturally Complex Polymers

Petra Bačová[†,‡] and Angel J. Moreno[*,¶,‡,§]

Departamento de Física de Materiales, Universidad del País Vasco (UPV/EHU), Apartado 1072, 20080 San Sebastián, Spain, Materials Physics Center MPC, Paseo Manuel de Lardizabal 5, 20018 San Sebastián, Spain, Centro de Física de Materiales (CSIC, UPV/EHU), Paseo Manuel de Lardizabal 5, 20018 San Sebastián, Spain, and Donostia International Physics Center, Paseo Manuel de Lardizabal 4, 20018 San Sebastián, Spain

E-mail: wabmosea@ehu.es

Abstract

By means of large-scale molecular dynamics simulations, we investigate branchpoint motion in pure branched polymers and in mixtures of stars and linear chains. We perform a purely geometrical density-based cluster analysis of the branchpoint trajectories and identify regions of strong localization (traps). Our results demonstrate that the branchpoint motion can be described as the motion over a network of traps at the time scales corresponding to the reptation regime. Residence times within the traps are broadly distributed, even extending to times much longer than the side arm relaxation time. The distributions of distances between consecutively visited traps are very similar for all the investigated branched polymers, even though

[*]To whom correspondence should be addressed
[†]Departamento de Física de Materiales, Universidad del País Vasco (UPV/EHU), Apartado 1072, 20080 San Sebastián, Spain
[‡]Materials Physics Center MPC, Paseo Manuel de Lardizabal 5, 20018 San Sebastián, Spain
[¶]Centro de Física de Materiales (CSIC, UPV/EHU), Paseo Manuel de Lardizabal 5, 20018 San Sebastián, Spain
[§]Donostia International Physics Center, Paseo Manuel de Lardizabal 4, 20018 San Sebastián, Spain

tube dilation is much stronger in the star/linear mixtures than in the pure branched systems. Our analysis suggests that the diffusivity of the branchpoint introduced by hierarchical models must be understood as a parameter to account for the effective friction associated to the relaxed side arm, more than the description of a hopping process with a precise time scale.

1 Introduction

The celebrated tube model for relaxation of entangled linear polymers[1,2] has been modified in recent years to describe the slow relaxation processes occuring in architecturally complex, branched polymers.[3–6] The presence of even a single branchpoint in the macromolecular architecture dramatically slows down the overall relaxation of the material. Because of the ubiquity of branchpoints in industrial polymers, the development of predictive tube models for the rheological properties of these materials has become a challenging field in both fundamental and applied polymer science.[3,7]

Different versions of hierarchical tube models have been introduced to account for the complex relaxation of entangled branched polymers.[5,6,8] These models postulate new mechanisms for relaxation of the intramolecular degrees of freedom. The polymer arms relax by deep contour length fluctuations (arm retraction[9]) from the outer segments to the branchpoint. This mechanism leads to an exponential distribution of relaxation times along the arm countour. As a consequence, the inner segments close to the branchpoint do not experience entanglements with the outer ones, which have relaxed at much earlier time scales. This constraint-release mechanism is known as dynamic tube dilution (DTD),[9–11] and leads to an effectively time-dependent, wider tube for the inner segments. After full relaxation of the arm, the branchpoint probes the space liberated by the removed constraints, and consequently it is assumed to perform diffusive steps (hops).[5,12] In asymmetric structures (e.g., T- and Y-stars, combs...), the main backbone is not yet relaxed at the time scale of relaxation of the side arms. Then branchpoint longitudinal diffusion proceeds along the backbone tube, the relaxed side arms act as effective 'frictional beads', and stress relaxation is completed by reptation of the backbone.[13–15]

Though the former qualitative picture has gained general acceptance, the specific details of the proposed mechanisms are controversial. It is commonly believed that inconsistencies originate from an inaccurate description of the relaxation in the neighborhood of the branchpoint. For instance, in order to reproduce experimental rheological data, different versions of hierarchical tube models need to make different assumptions on the direction and length scale for branchpoint mo-

tion, this occurring in the original undilated or in the dilated tube.[16] Solving this controversy is a challenging problem, since direct experimental access to the branchpoint motion is hard to be achieved, and reported data are still scarce.[17] In a pioneer work, Zhou and Larson[12] bridged the gap between theory and experiment by performing molecular dynamics simulations of entangled T-star polymers. Visual inspection of the branchpoint trajectories revealed rather distinct features from inner segment motion in entangled linear chains. Whereas the central part of the linear chain formed a diffuse trajectory along the confined tube, the trajectories of the branchpoints in asymmetric stars exhibited localization regions. This feature was recognized as a signature of the hopping mechanism postulated by tube models. However, a detailed quantitative characterization of the branchpoint trajectories was missing.

In this article we shed light on the former questions. We extend results of Ref.[12] to other branched architectures than T-star polymers, as well as to star/linear mixtures, and explore much longer time scales (two decades more). By performing a, purely geometrical, density-based cluster analysis of the branchpoint trajectories, we identify regions of strong localization ('traps') and provide evidence of branchpoint hopping. We find that this is not characterized by well-defined single time and length scales, which indeed exhibit broad distributions. Still, the cluster analysis allows us to compute the typical distance between consecutively visited traps directly from the simulation data. The obtained distance between traps is later compared to the diameter of the dynamically dilated tube, which is also obtained from the simulation data in a model-independent fashion.[18,19] The analysis reveals the presence of strongly localized branchpoints at times much longer than the arm relaxation time, even in the case of very weakly entangled side arms. The distributions of distances between consecutively visited traps are very similar for all the investigated branched polymers, even though tube dilation is much stronger in the star/linear mixtures than in the pure branched systems. We discuss the consequences of our analysis on the interpretation of the branchpoint diffusivity introduced by tube models.

The article is organized as follows. In Section 2 we summarize the model and simulation details, that are exhaustively described in Refs.[18,19] The density-based cluster analysis of the branch-

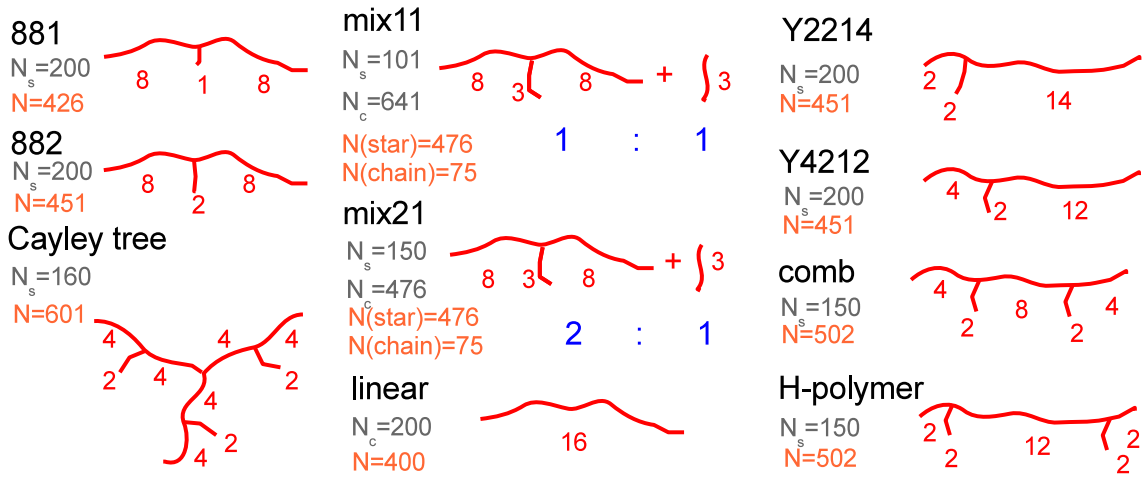

Figure 1: Scheme of the simulated systems: N_s represents the number of branched polymers and N_c the number of linear chains in the simulation box. N is the number of beads per macromolecule. The red numbers placed at each branch and backbone denote their lengths (Z) expressed in multiples of the entanglement length $N_e = 25$. Blue numbers express the composition of the mixtures, i.e. the ratio of the number of beads belonging to the asymmetric 883-stars to the total number of beads of the linear chains. In the text we refer to each particular system by its big black label.

point trajectories is presented in Section 3. Results from the analysis are presented in Section 4 and discussed in Section 5. Conclusions are given in Section 6.

2 Model and simulation details

We have performed large-scale molecular dynamics simulations of melts of architecturally complex polymers. These include T-shaped and Y-shaped asymmetric stars, H-polymers, two-arm combs and Cayley trees. In the case of the Cayley trees we analyze the motion of the three *outer* branchpoints. All the asymmetric branched polymers consist of a main backbone of $Z = 16$ entanglements. The three long arms of the Cayley trees have $Z = 8$ entanglements. In all cases the short arms are weakly entangled ($Z = 1$-3 entanglements). We have also simulated two mixtures (50%-50% and 67%-33% in monomer fraction) of T-stars with weakly entangled linear chains, as well as a system of pure linear chains of $Z = 16$. These are treated as two-arm stars, where the middle monomer is the 'branchpoint'. Details about the investigated systems are summarized in

Figure 1, including the number of entanglements in the arms and the backbone portions, and the number of polymers in the simulation box. The polymers are modelled by using the Kremer-Grest bead-spring model.[20] The monomeric units are represented as beads of mass m_0 interacting with a purely repulsive, cut-off Lennard-Jones (LJ) potential that accounts for the monomer excluded volume interaction:

$$U_{\mathrm{LJ}}(r) = \begin{cases} 4\varepsilon\left[\left(\frac{\sigma}{r}\right)^{12} - \left(\frac{\sigma}{r}\right)^{6} + \frac{1}{4}\right] & \text{for } r \leq 2^{1/6}\sigma, \\ 0 & \text{for } r > 2^{1/6}\sigma. \end{cases} \tag{1}$$

Connectivity between beads is provided by an elastic FENE potential:[20]

$$U_{\mathrm{F}}(r) = -\frac{1}{2}K_{\mathrm{F}}R_{\mathrm{F}}^2 \ln\left[1 - \left(\frac{r}{R_{\mathrm{F}}}\right)^2\right], \tag{2}$$

with spring constant $K_{\mathrm{F}} = 30\varepsilon/\sigma^2$ and maximum spring length $R_{\mathrm{F}} = 1.5\sigma$. The combination of Eq. (1) and Eq. (2) strongly limits the vibration of the bond connecting two beads, preventing chain crossability.[20] A bending potential given by

$$U_{\mathrm{bend}}(\theta) = k_\theta(1 - \cos\theta), \tag{3}$$

and with moderate strength ($k_\theta = 2\varepsilon$) is introduced to implement a slight degree of intramolecular stiffness. In the former equation, θ stands for the bending angle between three consecutive monomers. With this choice of the force field the entanglement length, $N_e \approx 25$ beads,[21] is considerably reduced respect to the case of fully flexible chains,[22] allowing us to simulate more strongly entangled systems with the same box size. Simulations were performed at temperature $T = \varepsilon/k_{\mathrm{B}}$ (with k_{B} the Boltzmann constant) and number density $\rho = 0.85\sigma^{-3}$ by using the free package ESPResSo.[23] The temperature was maintained constant by applying a Langevin thermostat with a friction constant $\Gamma = 0.5m_0/\tau_0$. The equations of motion were integrated by the velocity-Verlet algorithm with a time step $\Delta t = 0.01\tau_0$. The simulations typically extended over a few billion

time steps. A detailed description of the model and the equilibration and simulation procedure is given in Refs.[18] and.[19] In the following, times and distances will be given in the LJ-units of the model,[18–20] i.e., σ and $\tau_0 = (m_0\sigma^2/\varepsilon)^{1/2}$ for the distance and time, respectively.

3 Density-based cluster analysis

First we examine heterogeneous dynamics and deviations from Gaussian behavior of the branchpoint motion. The main panels of Figure 2 show the normalized van Hove self-correlation function, $4\pi r^2 G_s(r,t)$, of the branchpoint at two fixed times, namely $t = 2\times10^7$ (close to the end of the simulation) and $t = 2\times10^6$, in top and bottom panels, respectively. The inset in the top panel shows the time-dependence of the non-Gaussian parameter, $\alpha_2(t) = 3\langle\Delta r^4(t)\rangle/5\langle\Delta r^2(t)\rangle^2 - 1$ (this becomes zero in the limit of Gaussian behavior), where $\Delta r(t)$ is the displacement of the branchpoint at time t. To improve statistics, the former functions have been averaged over the branchpoint and the three nearest monomers in each of the arms stemming from the branchpoint. Though, within statistics, the non-Gaussian parameter seems to increase at times $t > 10^3$, this remains well below unity at the end of the simulation time window. This finding is rather different from the behavior $\alpha_2(t) > 1$ observed in strongly heterogeneous dynamic regimes, as e.g., the decaging regime in the vicinity of a glass transition.[24] The low values found for the non-Gaussian parameter of the branchpoints are consistent with the smooth shape of the van Hove functions, which do not exhibit neither secondary peaks nor long tails. These are also absent at the other simulation time scales not shown in Figure 2.

The former features suggest that there is not a well-defined, single length and/or time scale for branchpoint hopping (which otherwise would lead to a secondary peak in the van Hove function). Still, visual inspection of typical branchpoint trajectories gives evidence of strong localization of the branchpoint in certain regions of the space (‘traps’). The left frame (grey points) of Figure 3 shows a representative ‘smoothed’ trajectory of the branchpoint in the H-polymer. Smoothed trajectories are obtained as follows. In all the simulated systems the branchpoints are regularly saved

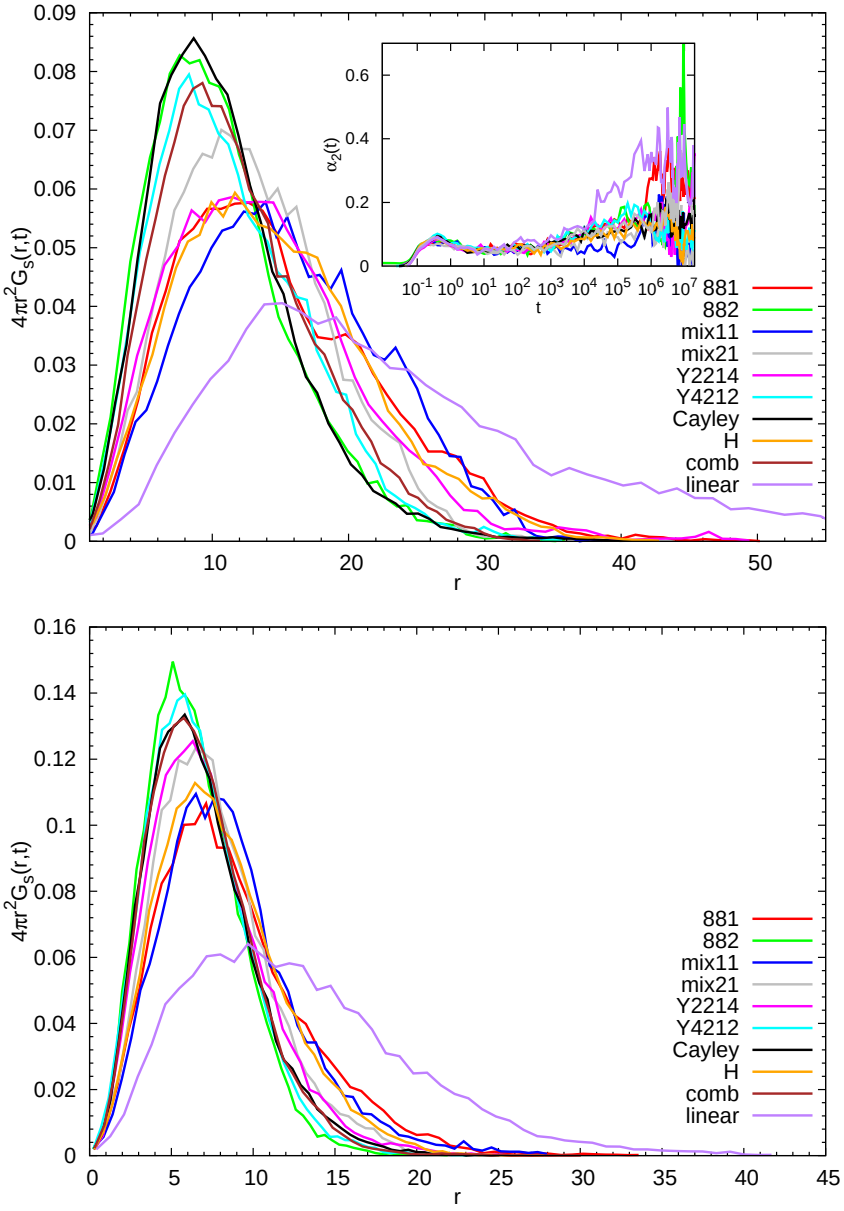

Figure 2: Normalized van Hove self-correlations functions for the branchpoints in the investigated systems, at time $t = 2 \times 10^7$ close to the end of the simulation (top) and at time $t = 2 \times 10^6$ (bottom). Inset in top panel: time-dependence of the non-Gaussian parameter of the branchpoints. Data sets for a same system are plotted with identical colors in the main panels and inset (see legend).

at every time interval of $\Delta t = 200$. Then each consecutive block of 10 positions is replaced by its averaged position $\mathbf{r}_{\rm av}$. The latter represents the average over a time interval $\Delta t = 2000$, which corresponds approximately to the entanglement time ($\tau_{\rm e} = 1800$).[12] The smoothed trajectory is constructed by taking all the averaged positions $\{\mathbf{r}_{\rm av}\}$, i.e, it represents the branchpoint trajectory

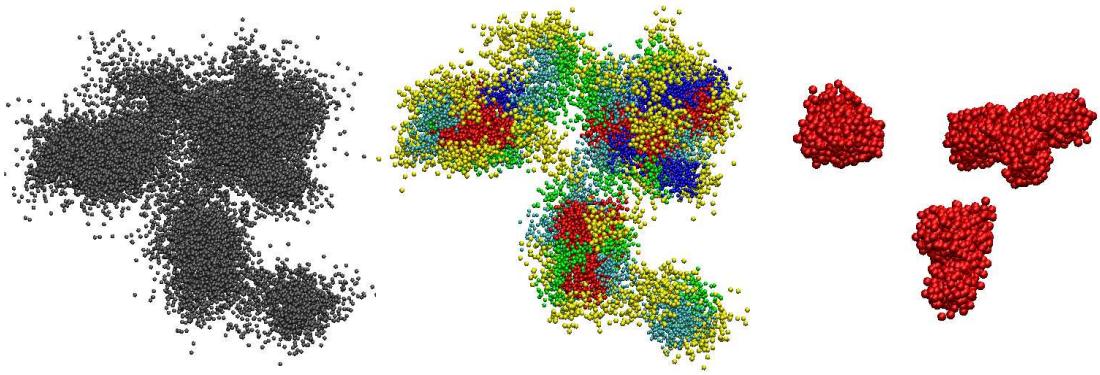

Figure 3: Illustration of the procedure for identification of the localization traps. Left frame: representative smoothed trajectory (see text) of the branchpoint of an H-polymer. Middle frame: the same trajectory after dividing the points into cells with different density of points $\rho_{\rm p}$, and removing the low-density cells. Different intervals of density are represented with different colors. Yellow: $1 \leq \rho_{\rm p} < 3$; green: $3 \leq \rho_{\rm p} < 4$; cyan: $4 \leq \rho_{\rm p} < 6$; blue: $6 \leq \rho_{\rm p} < 8$; red: $\rho_{\rm p} \geq 8$. The red points correspond to cells of density equal to or above the threshold value $\rho_{\rm th} = 8$, and are used to construct the clusters (right frame) representing the centers of the localization traps. The same representation scale is used in the three panels.

averaged over the local, fast Rouse-like vibrations occurring within the entanglement time. The total number of positions in the smoothed trajectory is of the order of 10^4 which, as mentioned above, covers a simulation time scale of $t \sim 2 \times 10^7$. As can be seen in the figure, the trajectory reflects the motion of the branchpoint over a collection of traps. However, there is not a clear separation between different traps. The character of the traps (dense or diffuse) and the shape of the trajectories change significantly between different systems and even within the same system.

Despite the fact that different traps are separated by ill-defined, diffuse interfaces, it is still possible to identify the centers of the traps. This can be done by performing a density-based cluster analysis of each trajectory. The underlying idea of this procedure is to solve regions of very high density of branchpoint positions, i.e, the regions in the trajectory that are more frequently visited by the branchpoint. This performs vibrations around the center of the trap, and occasionally jumps to another trap, where it is localized until it comes back to the original trap or moves to a new one. These wide vibrations and jumps lead to the diffuse, ill-defined interfaces separating the traps. The density-based cluster analysis identifies clusters of branchpoint positions at high-density regions

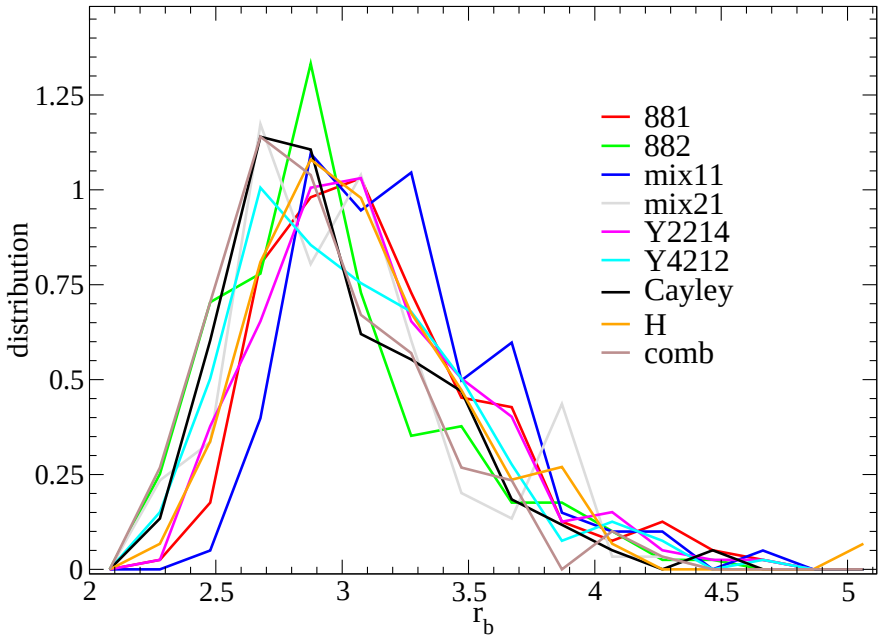

Figure 4: Distribution of the grid size r_b for the simulated systems.

of the trajectory, and removes the irrelevant low-density interfacial regions.

We use an algorithm based on the approach of Xu *et al.*[25] For every point in the trajectory we calculate the distance r_{nn} to its nearest neighbor point in the same trajectory. Then we construct a 3d-grid with bin size, r_b, identical to the *maximum* of all the r_{nn}-values obtained within the trajectory. Even for trajectories of a *same* system, the set of r_{nn}-values, and therefore also the value r_b of the bin size, will depend on each specific trajectory. The distribution of the r_b values for all the simulated systems is plotted in Figure 4. The specific value of the bin size r_b represents the size of the largest 'hole' that can be found within the considered trajectory. Thus, the whole trajectory can be mapped to a set of cells filled by points representing the branchpoint positions, and the empty cells do not form part of the trajectory.

Each point of the trajectory is assigned to the cell of the 3d-grid that contains its position. For each cell, of volume r_b^3, in the 3d-grid of a given trajectory, we define the local density of points, $\rho_p = n_p r_b^{-3}$, with n_p the number of trajectory points within the cell. We find that the local density of points is not homogeneously distributed along the trajectory. There are regions dominated by high-density cells separated by regions of low-density cells, the first ones corresponding to the cores of

the traps. This feature is illustrated in the middle frame of Figure 3, which shows, for the same trajectory of the left frame and in the same representation scale, branchpoint positions belonging to cells with density $\rho_{\rm p} \geq 1$. Different colors correspond to different ranges of density of the cells (see caption). The red points are located in the most dense cells, with $\rho_{\rm p} \geq 8$. The middle frame of Figure 3, by removing points in the low-density cells ($\rho_{\rm p} < 1$) that are visited by fast large-amplitude vibrations, nicely illustrates the formation of localization traps. It also demonstrates that the points in the cells of high density are not randomly distributed over the trajectory, but are organized into clusters.

We use the high-density clusters to identify the centers of the traps. First we fix a threshold density value $\rho_{\rm th}$ for *all* the branchpoint trajectories of a given system. Points in cells with local density $\rho_{\rm p} < \rho_{\rm th}$ are discarded for the cluster analysis. To select the threshold value $\rho_{\rm th}$ we first determine, for each cell in each trajectory, the *integer* part of the local density $\rho_{\rm p}^{\rm (int)} = {\rm int}(\rho_{\rm p})$. Second, we determine for each trajectory the maximum value of the former integer local densities, $\rho_{\rm p}^{\rm (i,max)} = \max\{\rho_{\rm p}^{\rm (int)}\}$. The obtained value of $\rho_{\rm p}^{\rm (i,max)}$, which is integer by construction, will be degenerate, i.e, there will be several cells in the trajectory with density $\rho_{\rm p} \geq \rho_{\rm p}^{\rm (i,max)}$. In order to warrant the selection of points for all the trajectories in the system, we define the threshold value $\rho_{\rm th}$ as the *minimum* of the $\rho_{\rm p}^{\rm (i,max)}$-values obtained for the different trajectories. Finally, for each trajectory we select all the branchpoint positions located at the cells with density $\rho_{\rm p} \geq \rho_{\rm th}$. We define the central regions of the traps as the clusters of such selected positions. Two of these selected positions in a same trajectory are assigned to a same cluster if they are at mutual distance $r \leq r_{\rm b}/2$, i.e., not larger than half the bin size of the 3d-grid of the trajectory. Likewise, two clusters merge into a single cluster if some point of one of the two clusters is at a distance $r \leq r_{\rm b}/2$ from some other point of the other cluster. The right frame of Figure 3 shows the high-density clusters ($\rho_{\rm p} \geq \rho_{\rm th}$), obtained by the former procedure, that correspond to the full trajectory of the left frame. The density-based cluster analysis provides well-defined separated trap centers for branchpoint localization.

4 Analysis of the time and length scales for branchpoint motion

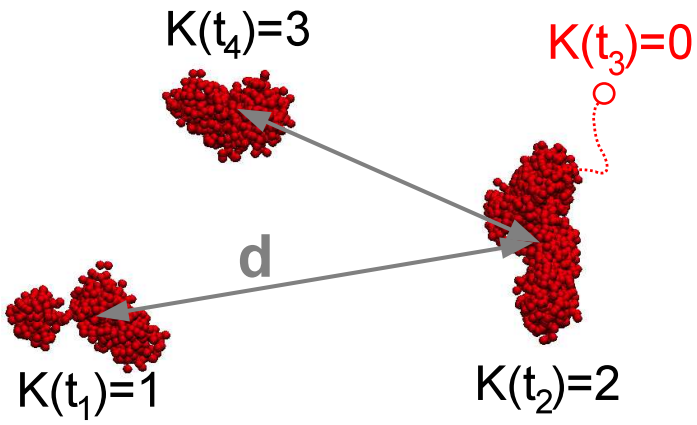

Figure 5: Scheme of the motion of the branchpoint between traps. The grey arrows indicate the distances between the centers-of-mass of the corresponding high-density clusters. The red dashed line with the red circle illustrates a fluctuation of the branchpoint out of the trap.

Once we have indentified the high-density clusters in every trajectory of the simulated systems, we analyze the motion between traps. We consider that a point of a given trajectory is in a trap if it belongs to one of the high-density clusters (i.e., $\rho_{\mathrm{p}} \geq \rho_{\mathrm{th}}$) defined above. If it is not the case, we consider that it belongs to one of the 'transient' intervals corresponding to the diffuse interfaces separating the traps. In this way each trajectory can be mapped to a time-dependent discontinuous function $K(t)$, where $1 \leq K \leq n_{\mathrm{t}}$ is an index denoting each of the n_{t} traps in the trajectory, and t is a discrete time variable denoting the saved points of the trajectory (see above). If the time t belongs to one of the transient intervals, $K(t) = 0$. In Figure 5 one simple case of the branchpoint motion between three traps is schematically depicted. In this scheme, the branchpoint is placed at time t_1 in the first trap ($K(t_1) = 1$), at time t_2 it moves to the second trap ($K(t_2) = 2$), at time t_3 it escapes from the second trap ($K(t_3) = 0$), and finally at time t_4 it is placed in the third trap ($K(t_4) = 3$).

Figure 6 represents a typical realization of $K(t)$ for the H-polymer. Only data with $K(t) > 0$ are shown, i.e., the transient intervals ($K(t) = 0$) appear as blank spaces blinking between the intervals in the traps (blue symbols). During a transient interval the branchpoint makes excursions

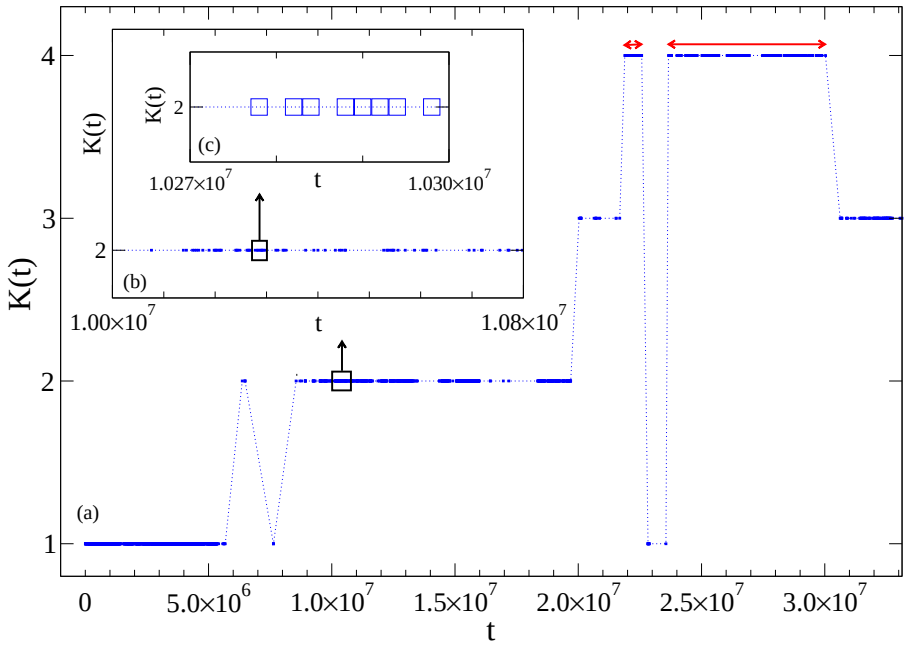

Figure 6: Time evolution of the trap index $K(t)$ for a typical branchpoint trajectory of the H-polymer with four different traps. Symbols for $K(t) = 0$ are not shown. Thus, transient intervals appear as blank spaces blinking within or between residence intervals. Dotted lines are guides for the eyes. The red double-arrows indicate two residence intervals in the trap K=4, separated by a visit to the trap K=1. Main panel (a): whole trajectory. Insets (b) and (c): selected intervals, as indicated by squares with arrows. The symbol size in the inset (c) corresponds to the time resolution of the trajectory $\Delta t = 2000$. To facilitate visualization, symbols sizes in (a) and (b) are bigger than Δt, so they frequently hide short transient intervals, as illustrated by passing from (a) to (b) and from (b) to (c).

out of the current trap, finally coming back to the same trap or moving to another one. We define a transient interval $[t_i, t_j]$, of duration $\tau_t = t_j - t_i$, in the discrete time sequence of a branchpoint trajectory, as that obeying the conditions: i) $K(t) = 0$ for $t_i \leq t \leq t_j$, ii) $K(t_{i-1}) \neq 0$, and iii) $K(t_{j+1} \neq 0)$. We define a residence interval of a branchpoint in a given trap k as an interval $[t_0, t_\mathrm{f}]$, of duration $\tau_\mathrm{r} = t_\mathrm{f} - t_0$, with the conditions: i) $K(t_0) = K(t_\mathrm{f}) = k$, ii) $K(t) = k$ or 0 for $t_0 < t < t_\mathrm{f}$, iii) $K(t') \neq k$ at the largest $t' < t_0$ for which $K(t') \neq 0$, and iv) $K(t'') \neq k$ at the smallest $t'' > t_\mathrm{f}$ for which $K(t'') \neq 0$. Therefore, two times t_k, t_l for which the branchpoint is in the *same* trap k belong to *different* residence intervals if there is, at least, one time $t_k < t < t_l$ at which the branchpoint visits another trap $k' \neq k$. Otherwise ($K(t) = k$ or 0 for $t_k < t < t_l$), they will belong to the same residence interval.

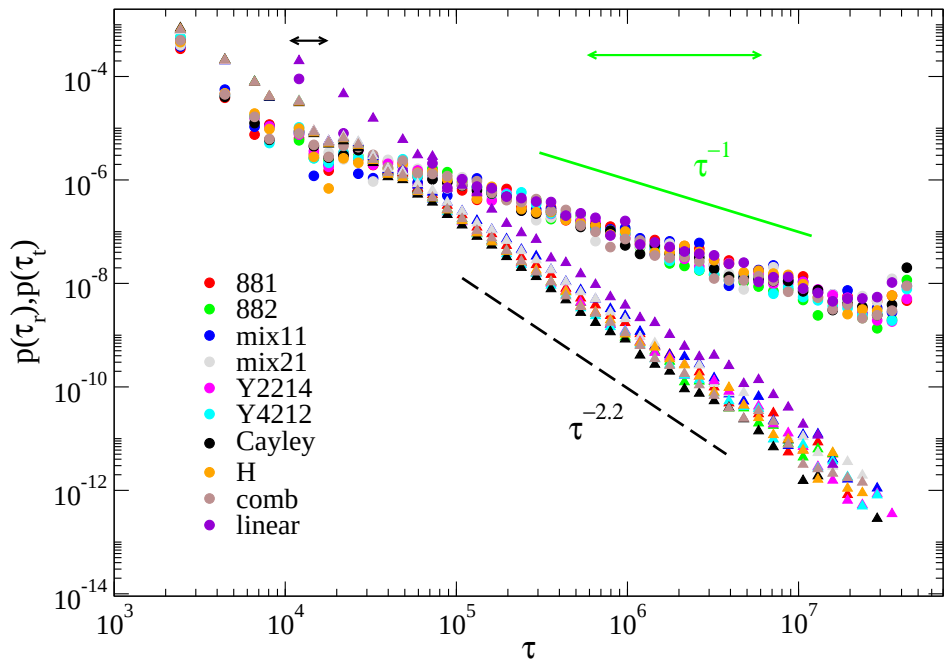

Figure 7: Distributions of residence times (circles) and transient times (triangles). Circles and triangles with identical colors correspond to the same simulated system (see legend). The lines indicate approximate power-law behavior (exponents are indicated). The black double-arrow indicates the range of values obtained for the average transient time. The green double-arrow indicates the approximate range for the onset of the apparent reptative regime in the MSD of the branchpoint (see below).

Figure 7 shows the distributions $p(\tau)$ of transient and residence times for all the simulated systems. We find extremely broad distributions, that can be approximated by power laws, $p(\tau) \sim \tau^{-2.2}$ and τ^{-1} for the transient and residence times respectively. We estimate the average transient time as $\langle \tau_t \rangle = \int \tau_t p(\tau_t) d\tau_t / \int p(\tau_t) d\tau_t$, finding values, for all the simulated systems, of the order of $\langle \tau_t \rangle \sim 10^4$, i.e, about 5 entanglement times. The distribution of transient times shows a much faster decay than the distribution of residence times. This indicates that most of the transient intervals correspond to fast explorations of the interfacial regions, before coming back to the original trap or moving to another one. Long explorations are very unfrequent events. Unfortunately we cannot estimate, in a similar manner, an average residence time, $\langle \tau_r \rangle$, from the data in Figure 7. Whereas the long-time contribution of $p(\tau_t)$ is already negligible at the end of the simulation window, in the former integrals for computing $\langle \tau_t \rangle$, it is not the case for $p(\tau_r)$. Indeed, the observed power-

law $p(\tau_r) \sim \tau_r^{-1}$ cannot be extrapolated to arbitrarily long times since this would lead to divergent values of $\langle \tau_r \rangle$. A correct estimation of $\langle \tau_r \rangle$ would require the knowledge of $p(\tau_r)$ beyond the simulation window. Still, by integration over the simulation window, we can determine a lower bound for $\langle \tau_r \rangle$ of the order of 5×10^6.

Though the common *scaling* $p(\tau_r) \sim \tau_r^{-1}$ is evident, the *overlap* of all the distributions $p(\tau_r)$ is an artifact of the used normalization $\int p(\tau_r) d\tau_r = 1$, where the integral is limited to the simulation window. The scaling $p(\tau_r) \sim \tau_r^{-1}$ will break down (changing to a steeper behavior) at times beyond the simulation window. We expect that the corresponding crossover will strongly depend on the system, occurring at later times for the systems with more entangled side arms.

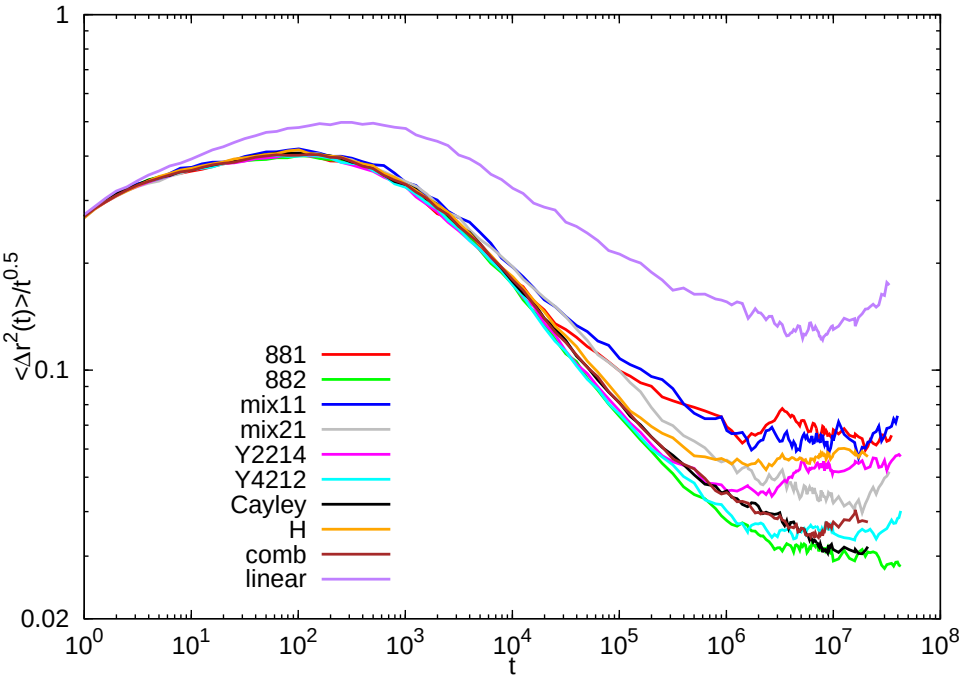

Figure 8: Mean-squared displacement of the branchpoint, divided by $t^{1/2}$, for the simulated systems.

Figure 8 shows the MSD of the branchpoint, normalized by $t^{1/2}$, for all the investigated systems. As for the van Hove function (see above), statistics have been improved by averaging over the branchpoint and the three nearest monomers in each of the arms stemming from the branchpoint. At times in the range of $t \sim 6 \times 10^5$ to 6×10^6 (depending on the system), the ratio $\langle \Delta r^2(t) \rangle / t^{1/2}$

for the asymmetric branched polymers shows a crossover to an apparent horizontal plateau. This is consistent with reptational motion of the main backbone (for pure reptation [1] $\langle \Delta r^2(t) \rangle \sim t^{1/2}$), which is expected at time scales after full relaxation of the side arms (this is not the case for the Cayley tree, where relaxation is completed by retraction[18]). If reptation of the branchpoint (or retraction in the case of the Cayley tree) is interpreted as a diffusion over a collection of traps, the time scale for the diffusive step has an extremely broad distribution, as reflected in Figure 7. The *beginning* of the reptation regime in the MSD of the branchpoint is dominated by the fastest branchpoints, which have explored more traps (with shorter residence times). However, there are branchpoints that are still residing in their original traps over time scales longer than the onset of reptation in the MSD, and obviously much longer than the relaxation time τ_a of the side arm — the lower bound estimated for $\langle \tau_r \rangle = 5 \times 10^6$ (see above) is indeed much larger than τ_a (see Table 1). This long-lived traps arise even in the 881-stars ($\tau_a \sim 4 \times 10^4$) where the length of the side arm is just one entanglement.

Table 1: Values of ρ_{th}, τ_a, $\Phi(\tau_a)$ and dilated tube diameter a (for dilution exponents $\alpha_d = 1$ and 4/3) obtained for all the branched systems.[19] For the linear chains we find a much lower threshold density, $\rho_{th} = 2$.

system	ρ_{th}	τ_a	$\Phi(\tau_a)$	$a(\alpha_d = 1)$	$a(\alpha_d = 4/3)$
881	8	37000 ± 9000	0.849 ± 0.011	9.68 ± 0.20	9.95 ± 0.23
882	17	439000 ± 65000	0.685 ± 0.013	10.78 ± 0.26	11.48 ± 0.31
mix11	6	962000 ± 265000	0.278 ± 0.021	16.96 ± 0.89	21.02 ± 1.37
mix21	10	1193000 ± 221000	0.373 ± 0.014	14.62 ± 0.49	17.23 ± 0.69
Y2214	10	308000 ± 56000	0.692 ± 0.013	10.73 ± 0.26	11.41 ± 0.31
Y4212	15	349000 ± 80000	0.678 ± 0.009	10.83 ± 0.23	11.56 ± 0.27
Cayley	13	360000 ± 87000	0.623 ± 0.018	11.30 ± 0.33	12.23 ± 0.42
H	8	275000 ± 39000	0.632 ± 0.006	11.22 ± 0.22	12.11 ± 0.25
comb	14	401000 ± 57000	0.593 ± 0.010	11.59 ± 0.27	12.64 ± 0.33

The fact that hopping between the traps may occur at times much longer than the side arm relaxation time, even if the side arm is very weakly entangled, might question the usual interpretation of the branchpoint diffusivity D in hierarchical tube models. Actually, this intervenes in the model to effectively account for the friction associated to the relaxed side arm,[19] this friction affecting the time scale for the ultimate relaxation of the backbone by reptation. Our analysis suggests that

it should be understood just in this (pragmatic) way, and not as describing a hopping motion with a precise characteristic time scale. In its original definition, the branchpoint diffusivity is given by $D = p^2 a_0^2 / 2\tau_a$, with a_0 the original undilated tube diameter and p^2 (hopping parameter) some dimensionless factor. More elaborated expressions of D in hierarchical models (see, e.g., a recent review in Ref.[19]) introduce corrections to account for, e.g., hopping in the dilated tube and backbone frictional contributions. In all cases the hopping time scale is given by τ_a. Our analysis shows that this assumption is not justified and that the definition of a precise hopping time in itself has no major physical significance.

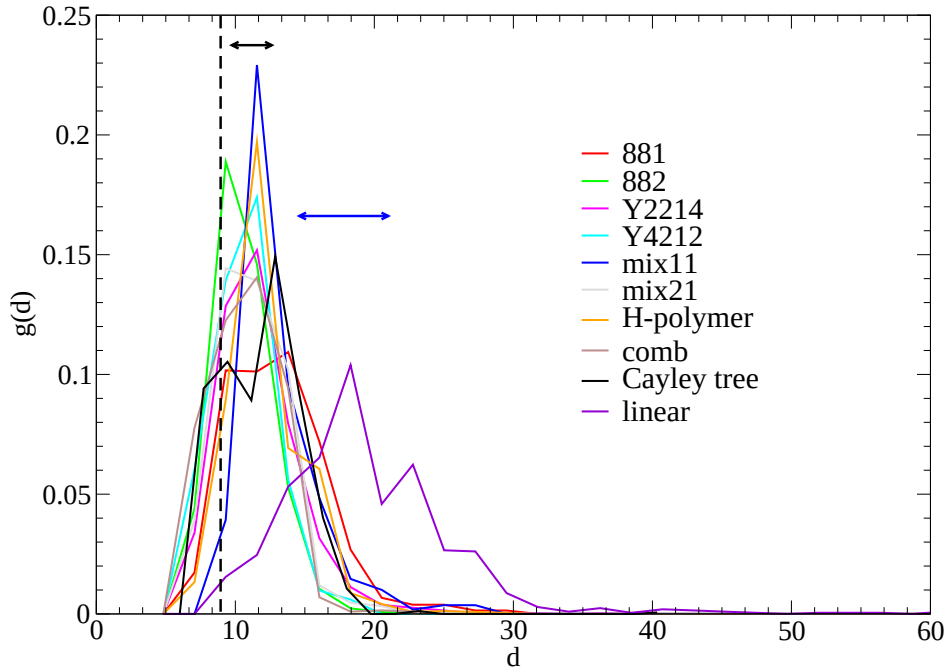

Figure 9: Distribution of distances between consecutively visited traps for all the studied systems (see legend). The vertical dashed line indicates the original undilated tube diameter. The double-arrows comprise the range of dilated tube diameters reported in Table 1 for the pure branched systems (black double-arrow) and the star/linear mixtures (blue double-arrow).

The function $K(t)$ provides for each branchpoint the temporal sequence of visited traps. This allows us to compute distances between *consecutively* visited traps. We define such distances as the distances between the centers-of-mass of the corresponding high-density clusters (see Figure 5). Figure 9 shows, for all the simulated systems, the distribution of distances $g(d)$ between consec-

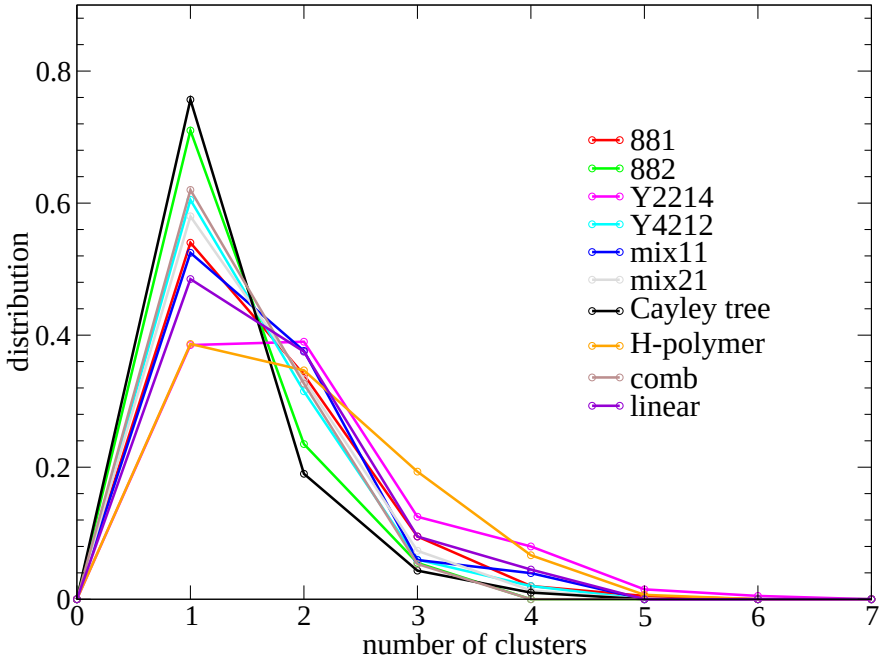

Figure 10: Distribution of the number of traps per branchpoint trajectory in the investigated systems.

utively visited traps. The data in Figure 9 have limited statistics. This is a consequence of two factors. First, the number of branchpoints per simulation box is relatively small (a few hundreds). Second, the trajectories show a small number of traps (less than 7 per trajectory), which unavoidingly leads to a reduced number of distances. The distribution of the number of traps per trajectory is shown in Figure 10. Good statistics for the distributions in Figure 9 would only be achieved by extending considerably the time scale of the simulations (to increase the number of traps per trajectory and the corresponding number of distances). However, this would be beyond the limit of current supercomputation resources. We have indeed employed an unusual amount of CPU time, about 3.5 million core-hours, for the present work. In spite of their limited statistics, the distributions for all pure branched polymer melts and star/linear mixtures in Figure 9 unambiguosly exhibit a clear, broad peak centered at a distance $d \sim 11$. The broad character of the peak is consistent with the absence of a well-defined, single length scale for hopping, as anticipated by inspection of the van Hove function in Figure 2. The distribution of the distances between the traps for the linear chain is much broader and shifted to longer distances. However, we do not give a major physical

significance, in terms of 'hopping', to the results for the linear chain, since traps there have very low densities (the threshold density $\rho_{\mathrm{th}} = 2$ is much lower than for the branched systems and for the mixtures, see Table 1). Traps for the linear chains are also much more sparse, as demonstrated by computing the distribution of radii of gyration of the high-density clusters (Figure 11). Both the much lower density and larger size of the traps in the linear chains are a consequence of the faster and broader back-and-forth motions of the 'branchpoint', which does not have to drag a side arm during its reptative motion. Thus, branchpoint trajectories for the linear chains are very diffuse and traps do not reflect a real localization of the branchpoint.

As explained above, the cluster analysis is based on preselecting branchpoint positions that are located in cells with density above a threshold value, $\rho_{\mathrm{p}} \geq \rho_{\mathrm{th}}$. The latter is strongly dependent on the system. It varies from $\rho_{\mathrm{th}} = 6$ in the mixture mix11 to $\rho_{\mathrm{th}} = 17$ in the 882-stars (see second column in Table 1). Having noted this, it must be stressed that the obtained distributions of distances (regarding the location of the peaks) are not affected within statistics whatever reasonable choice of ρ_{th} is made. We find very similar results by using, for each system, a threshold density about 25 % lower than the respective value given in Table 1. The clusters of points in the high-density cells ($\rho_{\mathrm{p}} \geq \rho_{\mathrm{th}}$) tend to be surrounded also by dense cells. Using a lower threshold density, $\rho'_{\mathrm{th}} < \rho_{\mathrm{th}}$, increases the number of points per cluster. However, this rarely leads to merging of the original clusters, provided that ρ'_{th} is high enough to remove the low-density cells. Thus, the original number of clusters (obtained for ρ_{th}) is not significantly altered. Moreover, the higher population of the clusters for ρ'_{th} does not significantly change either the original distribution of distances found for ρ_{th}, because the centers-of-mass of the clusters are dominated by the contribution of the highest density cells. This is demonstrated in Figure 12, where we plot the distribution of the distances between the traps for two threshold densities: the one listed in Table 1 (ρ_{th}) and ρ'_{th} that is 25% lower than ρ_{th}. In summary, the algorithm used here provides a sound, robust method for identifying localization traps and distances between the traps in architecturally complex polymers.

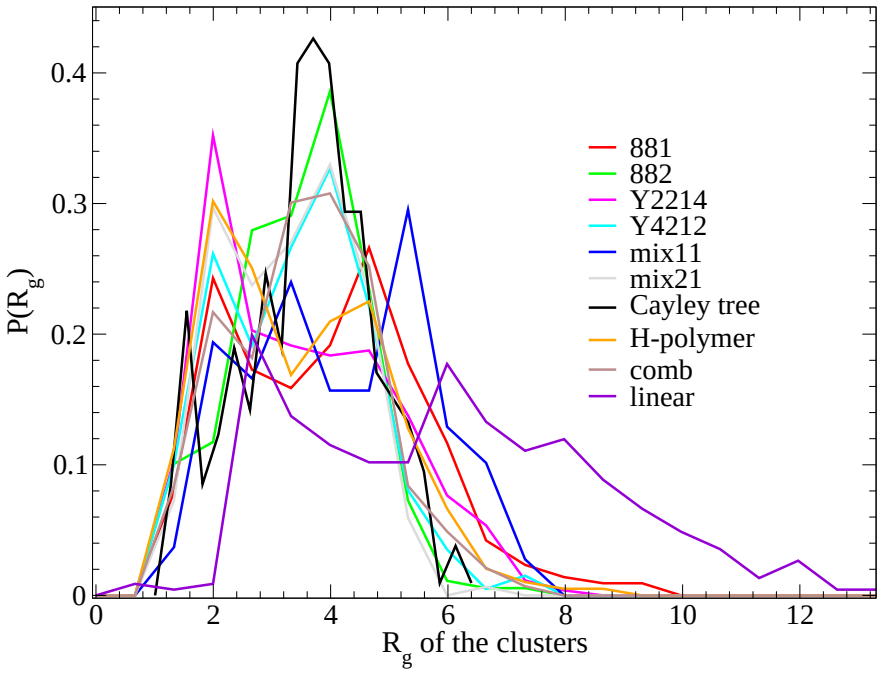

Figure 11: Distribution of the radii of gyration of the traps in the investigated systems.

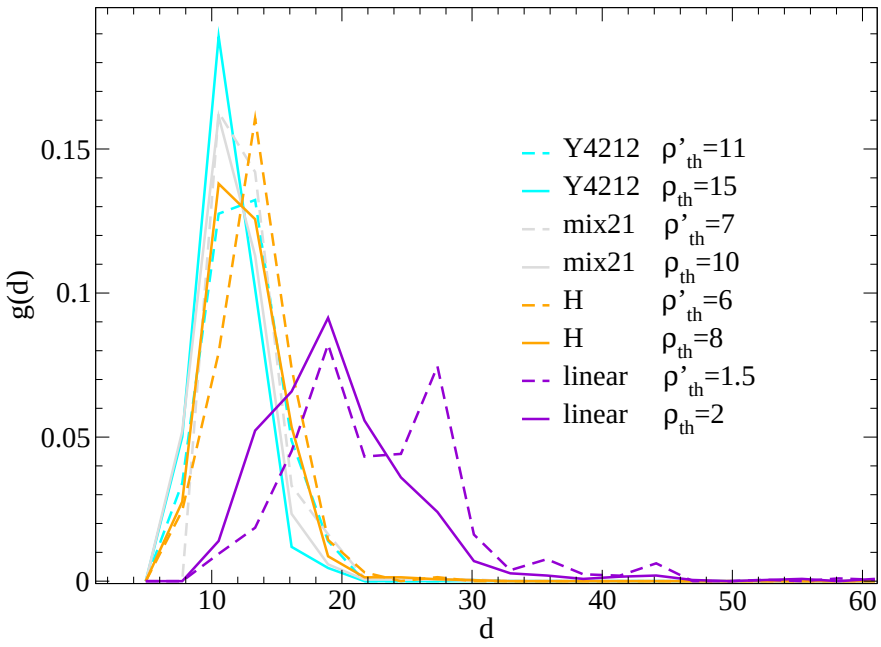

Figure 12: Distribution of distances between consecutively visited traps for two different threshold densities chosen for some representative systems. The data from Figure 9 (ρ_{th}) are plotted with full lines. The dashed lines are results for the threshold densities $\rho'_{\text{th}} \approx 0.75\rho_{\text{th}}$.

5 Discussion

We confront the former characterization of the traps with predictions of tube models. Within the dynamic tube dilution (DTD) hypothesis, the diffusive step of the branchpoint in the tube is given by the value of the dilated tube diameter, a, at the longest relaxation time of the side arm, $\tau_{\rm a}$:[2,9]

$$a = a_0 \Phi^{-\alpha_d/2}(\tau_{\rm a}). \tag{4}$$

The original undilated tube diameter, a_0, takes a value $a_0 = 8.92 \pm 0.13$ for the simulated model.[19,21] The function $\Phi(t)$ is the tube survival probability, and α_d is the exponent for dilution of the entanglement network. The latter is assumed to take a value $\alpha_d = 1$ or $\alpha_d = 4/3$.[9] Without invoking model-dependent outputs from tube theories, the tube survival probability can be independently computed from the simulation data. This is obtained by analyzing the correlation function of the tangent vectors of the chain. The relaxation time $\tau_{\rm a}$ is obtained by analyzing the decay of the end-to-end correlation function of the side arm. The procedure for computing $\Phi(t)$ and $\tau_{\rm a}$ has been described in detail in Ref.[19] Table 1 shows the values of $\Phi(\tau_{\rm a})$ obtained for all the simulated systems, as well as the corresponding values at $\tau_{\rm a}$ of the dilated tube diameter a. The latter is obtained from Eq. (4) for both values of the dilution exponent $\alpha_d = 1$ and 4/3. The dilated tube diameter for the pure branched polymers ranges from 9.7 (for 881-stars with $\alpha_d = 1$) to 12.6 (for combs with $\alpha_d = 4/3$). The strength of dynamic tube dilution for branchpoint hopping is related to the fraction of relaxed material at the time $\tau_{\rm a}$. As discussed in Ref.[19] and consistently with results in Table 1, the former fraction grows by increasing the length and the number of the side arms. Therefore, since the dilated tube diameter is inversely proportional to $\Phi^{\alpha_d/2}(\tau_{\rm a})$, dilation is stronger for the simulated stars with side arms of $Z = 2$ entanglements than for the 881-stars. Likewise, the dilated tube is wider for the simulated combs and H-polymers than for the stars. Because of the high concentration of short chains (of same $Z = 3$ as the side arms of the stars) in the star/linear mixtures, tube dilation is much stronger than in the pure systems. Thus, in the mixture mix11 the dilated diameter is $a = 17$ and 21 for $\alpha_d = 1$ and 4/3, respectively.

In spite of the limited statistics of the distributions in Figure 9, the peaks are clearly centered at distances larger than the original undilated tube diameter $a_0 \approx 9$. The centers of the peaks in the pure branched systems are consistent with the range of values (indicated by the black double-arrow) reported in Table 1 for the dilated tube diameter. However, this is not the case for the star/linear mixtures, whose distributions $g(d)$ are hardly distinguishable from those of the pure branched systems, and centered at values much smaller than the range of expected dilated diameters (blue double-arrow). The interpretation of these results is not obvious. It might be that the apparent agreement between the dilated tube diameter and the maximum of $g(d)$ for the pure branched systems is fortuitous, as suggested by the strong disagreement in the case of the mixtures. The coincidence (within statistics) of both the distributions $g(d)$ and the scaling of $p(\tau_r)$ suggests instead a common picture for all the branched polymers in the pure state and in the mixtures. Namely, long-time reptation of the branchpoint occurs via motion over a network of traps with very similar static properties. Dynamic differences between the long-time dynamics of the different systems are related to the different frequency of the hops (note that, as discussed above, the respective distributions $p(\tau_t)$ are *different* since the scaling $p(\tau_t) \sim \tau_t^{-1}$ will break down at different times for each system). This different frequency originates from the different effective friction associated to the side arm in each system .

In summary, the analysis of residence times and distances between traps reveals two interesting results:

i) The absence of a characteristic time scale for branchpoint hopping, together with the presence of long-living traps far beyond the arm relaxation time. Hence, the branchpoint diffusivity introduced by hierarchical models should be understood as an effective description of friction, relevant for reptation of the backbone and associated to the drag of the relaxed side arms, and not as the description of a hopping motion with a characteristic time scale. The fact that, the average residence times within the traps seem to be indeed much longer than the time scale (τ_a) assumed by the hierarchical models, is compensated by the actual values found for the hopping parameter, much

lower[19] than the naive value $p^2 \sim 1$ originally proposed.

ii) The apparent independence of the typical hopping distance on the strength of dynamic tube dilution. As discussed in Refs.,[18,19] the mechanism of DTD seems to be essential to describe localization of the branchpoint during retraction of the side arm, and to account for the effective friction exerted by the relaxed side arms. However, long-time reptation seems to occur more along a partially dilated tube (similar in all investigated systems) than along that expected from DTD.

6 Conclusions

We have performed large-scale simulations of melts of entangled pure branched polymers, as well as of star/linear mixtures. By performing a density-based cluster analysis of the branchpoint trajectories, we have identified localization traps and characterized typical diffusive steps for branchpoint motion. We find that these are characterized by broad distributions of time and length scales. Our method does not invoke tube-based model dependent assumptions. It is based on a purely geometric approach, providing information on branchpoint dynamics by a direct real-space analysis of the trajectories. The branchpoint motion can be seen as the motion over a network of traps at the time scales corresponding to the reptation regime. The analysis reveals some unexpected results. Residence times within the traps are broadly distributed, even extending to times much longer (by decades) than the side arm relaxation time. This feature is observed even in the case of very weakly entangled side arms. The distributions of distances between consecutively visited traps are very similar for all the investigated branched polymers, even though tube dilation (induced by DTD) is much stronger in the star/linear mixtures than in the pure branched systems. Whether these results are compatible with the current versions of hierarchical models is an open issue. Our analysis suggests that the diffusivity of the branchpoint introduced by hierarchical models must be understood as a parameter to account for the effective friction associated to the relaxed side arm, and not as a description of a hopping process with a precise time scale (which definitely does not correspond to

the side arm relaxation time).

7 Acknowledgements

We acknowledge support from projects FP7-PEOPLE-2007-1-1-ITN (DYNACOP, EU), MAT2012-31088 (Spain) and IT654-13 (GV, Spain). We acknowledge the programs PRACE, HPC-Europa2 and ESMI (EU), and ICTS (Spain) for generous allocation of CPU time at GENCI (France), HLRS and FZJ-JSC (Germany) and CESGA (Spain). We thank D. J. Read, C. Das and C. Tzoumanekas for useful discussions.

References

(1) Doi, M.; Edwards, S. F. *The Theory of Polymer Dynamics*; Oxford University Press, USA, 1986.

(2) McLeish, T. C. B. *Advances in Physics* **2002**, *51*, 1379–1527.

(3) Read, D. J.; Auhl, D.; Das, C.; den Doelder, J.; Kapnistos, M.; Vittorias, I.; McLeish, T. C. B. *Science* **2011**, *333*, 1871–1874.

(4) Larson, R. G. *Macromolecules* **2001**, *34*, 4556–4571.

(5) Das, C.; Inkson, N. J.; Read, D. J.; Kelmanson, M. A.; McLeish, T. C. B. *Journal of Rheology* **2006**, *50*, 207–234.

(6) Van Ruymbeke, E.; Bailly, C.; Keunings, R.; Vlassopoulos, D. *Macromolecules* **2006**, *39*, 6248–6259.

(7) Chen, X.; Costeux, C.; Larson, R. G. *Journal of Rheology* **2010**, *54*, 1185–1205.

(8) Park, S.; Shanbhag, S.; Larson, R. *Rheologica Acta* **2005**, *44*, 319–330.

(9) Milner, S. T.; McLeish, T. C. B. *Macromolecules* **1997**, *30*, 2159–2166.

(10) Marrucci, G. *Journal of Polymer Science* **1985**, *23*, 159–177.

(11) McLeish, T. C. B. *Journal of Rheology* **2003**, *47*, 177–198.

(12) Zhou, Q.; Larson, R. G. *Macromolecules* **2007**, *40*, 3443–3449.

(13) Frischknecht, A. L.; Milner, S. T.; Pryke, A.; Young, R. N.; Hawkins, R.; McLeish, T. C. B. *Macromolecules* **2002**, *35*, 4801–4820.

(14) McLeish, T. C. B. et al. *Macromolecules* **1999**, *32*, 6734–6758.

(15) Kirkwood, K. M.; Leal, L. G.; Vlassopoulos, D.; Driva, P.; Hadjichristidis, N. *Macromolecules* **2009**, *42*, 9592–9608.

(16) Wang, Z.; Chen, X.; Larson, R. G. *Journal of Rheology* **2010**, *54*, 223–260.

(17) Zamponi, M.; Pyckhout-Hintzen, W.; Wischnewski, A.; Monkenbusch, M.; Willner, L.; Kali, G.; Richter, D. *Macromolecules* **2010**, *43*, 518–524.

(18) Bačová, P.; Hawke, L. G. D.; Read, D. J.; Moreno, A. J. *Macromolecules* **2013**, *46*, 4633–4650.

(19) Bačová, P.; Lentzakis, H.; Read, D. J.; Moreno, A. J.; Vlassopoulos, D.; Das, C. *Macromolecules* **2014**, *47*, 3362–3377.

(20) Kremer, K.; Grest, G. S. *The Journal of Chemical Physics* **1990**, *92*, 5057–5086.

(21) Everaers, R.; Sukumaran, S. K.; Grest, G. S.; Svaneborg, C.; Sivasubramanian, A.; Kremer, K. *Science* **2004**, *303*, 823–826.

(22) Wang, Z.; Likhtman, A. E.; Larson, R. G. *Macromolecules* **2012**, *45*, 3557–3570.

(23) Limbach, H.; Arnold, A.; Mann, B.; Holm, C. *Computer Physics Communications* **2006**, *174*, 704 – 727.

(24) Bernabei, M.; Moreno, A. J.; Zaccarelli, E.; Sciortino, F.; Colmenero, J. *Journal of Chemical Physics* **2011**, *134*, 024523.

(25) Xu, X.; Ester, M.; Kriegel, H.-P.; Sander, J. **1998**, 324–331.

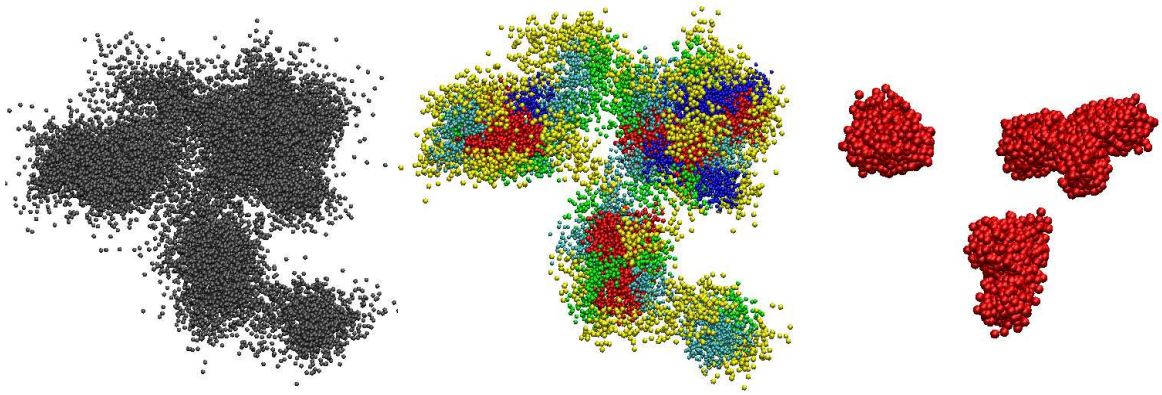

TABLE OF CONTENTS